



High speed remote laser cutting of electrodes for lithium-ion batteries: Anode



Dongkyoung Lee^a, Rahul Patwa^c, Hans Herfurth^c, Jyotirmoy Mazumder^{a,b,*}

^a Center for Lasers and Plasmas for Advanced Manufacturing (CLPAM), Department of Mechanical Engineering, University of Michigan, Ann Arbor, MI 48109, United States

^b Department of Material Science and Engineering, University of Michigan, Ann Arbor, MI 48109, United States

^c Fraunhofer Center for Laser Technology, 46025 Port Street, Plymouth, MI 48170, United States

HIGHLIGHTS

- ▶ A 3D mathematical model of the high speed remote laser cutting of anode is developed.
- ▶ Simulation results present depth, width, and absorptivity variations during the laser cutting of the anode.
- ▶ Temperature distribution, melt pool geometry, melt pool flow, and composition distribution are examined.
- ▶ The cut surface, kerf width, and copper composition of the experimentally obtained sample are measured and compared.
- ▶ Computational and experimental results show an agreement.

ARTICLE INFO

Article history:

Received 17 August 2012

Received in revised form

14 October 2012

Accepted 15 October 2012

Available online 10 November 2012

Keywords:

Remote laser cutting

Lithium-ion battery

Computational model

Anode

Single mode fiber laser

Experimental validation

ABSTRACT

Lithium-ion battery performance is affected by cut surface quality during the electrodes' cutting process. Currently, die cutting and rotary knife slitting have been used to cut prismatic and cylindrical electrodes, respectively. Both techniques, which require expensive tooling that wear out over time, result in process instability and poor cut quality. These will cause an internal short circuit and significant heat generation in the cells. Laser cutting, proved and widely utilized in the industry, can solve the abovementioned problems by improving cut surface quality due to many advantages, such as no tool wear, high energy concentration, fast processing speed, very narrow Heat Affected Zone, applicability to nearly all materials, and flexibility of laser power. Investigating underlying physical phenomena with numerical analysis provides significant advantages to fully utilize the remote laser cutting of electrodes for lithium-ion batteries. In this paper, a mathematical model of three-dimensional self-consistent remote laser cutting is presented for anode (graphite-coated copper) of lithium-ion batteries. Computational and experimental results, obtained by using laser power of 450 W and scanning speed of 5 m s^{-1} , show a two-step melt pool geometry and copper composition increase on the material interface.

© 2012 Elsevier B.V. All rights reserved.

1. Introduction

To reduce CO₂ emissions, the United States Environmental Protection Agency (EPA) set up stringent emission standards in 2009. To meet these stringent standards, automakers have focused heavily on the development of Hybrid Electrical Vehicles (HEVs), Electrical vehicles (EVs), and Plug-in Hybrid Electrical Vehicles (PHEVs). To develop these vehicles in a more efficient and environmentally friendly manner, an understanding of automotive

battery technology is essential. Among many of the battery technologies, the lithium ion battery represents the most promising technology due to its high energy-to-weight ratio, high power density, high energy density, and lighter weight than other energy-equivalent secondary batteries [1,2].

Much research has been focused on improving lithium ion battery performance: developments of electrode materials and battery manufacturing processes [3]. Many researchers have been focused on development of electrode materials. Broussely et al. [4] described a short historical perspective of positive materials by comparing battery performance parameters such as specific capacity. Recently, more attention has been given to cathode materials to improve capacity for lithium ion batteries through nanotechnology [5–8]. Furthermore, to improve the capacity of anode materials, silicon or silicon-based materials have been

* Corresponding author. Department of Mechanical Engineering, University of Michigan, Ann Arbor, MI 48109, United States. Tel.: +1 734 647 6824; fax: +1 734 763 5772.

E-mail address: mazumder@umich.edu (J. Mazumder).

suggested as potential alternatives for the next generation of lithium ion battery systems [9–13].

Although lithium ion battery manufacturing process is also an important issue, little research has been done in this area. From the manufacturing process of prismatic lithium ion cells, several problems have been reported during the slitting process. Currently, die cutting and rotary knife slitting have been used to cut the prismatic and cylindrical electrodes, respectively [14–16]. Both techniques require relatively expensive tooling that wears out over time. This tool wear results in process instability and requires additional cost and downtime to replace it. Furthermore, a redesign of mechanical cutting processes demanding extra expense is an inevitable step, since cell specifications vary depending on the application, such as electronic devices and electric vehicles. The most significant disadvantage due to the tool wear is the problem of inconsistent cut surfaces with defects, which are characterized by burrs, delamination, edge bending, and micro-sized material attachments, as shown in Fig. 1. These defects cause the penetration of the separator, giving rise to internal short circuits. Moreover, the quality of a poor cut surface makes electrodes susceptible to higher electrical stress, which can lead to significant heat generation and possible thermal runaway [17]. Internal short circuits and significant heat generation eventually can result in catastrophic failure of the entire system.

Laser cutting is proven and widely utilized in industry [18]. This highly efficient and reliable manufacturing method can solve the abovementioned problems since it has many advantages, such as no tool wear due to contact-free process, high energy concentration, low noise level, fast processing speed, very narrow Heat Affected Zone (HAZ), applicability to nearly all materials, and flexibility of laser power [18]. Most importantly, laser cutting is relatively easily applicable to different cell specifications with less

cost, since the redesign of laser cutting processes is relatively simpler and cheaper compared to the redesign of mechanical cutting processes.

While laser cutting has many advantages, the application of laser cutting to size the lithium ion batteries has been investigated by few researchers. The achievable cutting speeds and cut qualities of the electrodes for the lithium-ion battery have been studied with a pulsed solid state laser and a single mode fiber laser in combination with fixed optics and 2D scanning optics [15]. High speed laser cuttings of electrodes for the lithium-ion battery using single mode fiber lasers have also been investigated by Patwa et al. [16]. They illustrated the achievable highest cutting speed, the effect of the focus beam and the number of cutting passes. A comparison between a Continuous Wave (CW) laser and a pulsed laser cutting of electrodes for lithium-ion batteries has additionally been examined, and achievable cutting speeds, qualities, and the application areas for the two operating modes have been also discussed [19]. These experimental conclusions have been derived through a trial and error process [19]. Investigating underlying physical phenomena with numerical analysis provides significant impacts to fully utilize the remote laser cutting of electrodes for lithium-ion batteries. Since the understanding of physical phenomena for each material during laser cutting is an essential step prior to investigating the laser cutting of electrodes, numerical studies by Lee and Mazumder [20] of laser processing parameters on current collectors for lithium-ion batteries have been done. Thresholds of laser processing parameters, such as laser power and scanning speed for the laser cutting of current collectors, have been found. A mathematical model of laser cutting of an anode is developed in this paper. This paper is organized as follows.

First, a mathematical model of three-dimensional self-consistent laser cutting is depicted for anode of lithium-ion batteries. Second, an experimental set up and procedures are stated. Third, simulation results are analyzed in terms of penetration time, depth, width, and absorptivity. Furthermore, melt pool flow, melt pool geometry, and copper composition changes on the material interface are discussed. Fourth, experimental results are compared with simulation results. Finally, the conclusions drawn from this work are summarized.

2. Mathematical modeling

Laser cutting of an anode material includes interconnected physical phenomena. When a laser irradiates a substrate, the substrate absorbs light energy. This absorbed energy is enough to melt and evaporate materials. In the melted area, called the melt pool, solid and liquid materials coexist so that they form a mushy zone. Since this mushy zone consists of solid and liquid phases, thermo-physical material properties are changed based on the liquid and solid fraction.

In the evaporation interface, a very thin layer of several mean free paths is observed. This thin layer is called a kinetic Knudsen layer. Across the kinetic Knudsen layer, steep changes of temperature, pressure, and density occur, in which the continuum hypothesis fails. Thus, a mathematical discontinuity needs to be considered as a jump condition with back pressure [21]. Furthermore, mass and thermal energy loss on the interface are taken into account in this mathematical model through the jump condition [22].

In addition to the evaporation, there are other physical phenomena that can be observed at the Liquid/Vapor (L/V) interface. Vaporization behaves as a repulsive force on the melt pool, and is referred to as recoil pressure. This recoil pressure generates a narrow and deep penetration hole, called a keyhole or deep penetration hole. This keyhole changes the geometry of the L/V interface and absorbs more energy by internal multiple reflections

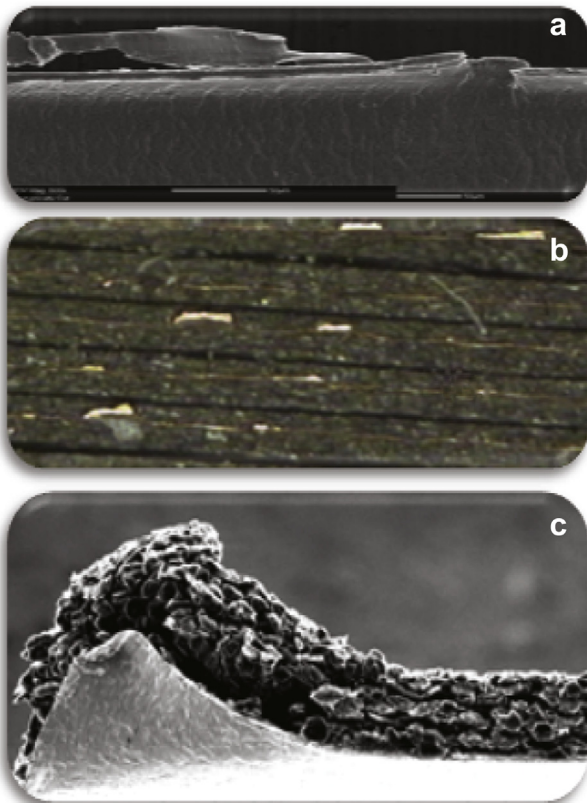


Fig. 1. Micro-sized material attachments (a), edge bending (b), and inconsistent cut quality (c).

[23]. Moreover, surface tension exists due to the geometry change and temperature gradient.

Different from single materials, electrodes are a sandwiched composite material. Due to this sandwiched shape, the interface of each material needs to be carefully considered. A material interface of the two sandwiched materials plays a significant role in the laser cutting of electrodes. On the material interface, melted materials are mixed and compositions change. These composition changes vary the mixture properties. A concentration equation is used to keep track of composition variation on the boundary of the current collector and active electrode materials during the laser cutting process. Material properties of the mixture on the boundary of the current collector and active electrode materials are realized with the aid of the phase diagram and the composition equation.

2.1. Assumptions

- Laminar, Newtonian, incompressible flow.
- Constant material properties.
- Graphite has no liquid phase.
- Laser beam has Gaussian distribution.
- Material properties between vapor and liquid are smoothed out for numerical purposes.
- Material properties for high temperature range are extrapolated.
- Phase diagram of copper and graphite is extrapolated.

2.2. Governing equations

An anode material consists of copper as a current collector and graphite as an active electrode material as shown in Fig. 2. Since graphite is sublimated, there exist two phases, solid and vapor, at the early stage of the simulation. To realize this sublimation characteristic of graphite, several modifications were made. Liquid viscosity is assumed to be high compared to the gas phase since the proposed mathematical model solves both liquid and gas phases. Moreover, liquid properties are set to be the same as solid properties, and surface tension is ignored.

However, once the depth of a deep penetration hole reaches the interface of graphite and copper, the liquid phase of copper and the solid phases of copper and graphite exist together. When this mushy zone is formed, composition varies at the interface. Thus, thermo-physical properties of solid and liquid mixtures of the two materials need to be carefully considered based on the composition changes and mass fractions of the two materials. To incorporate this mushy zone, this study adopted a method developed by Bennon and Incropera [24], which is an extension of the classical mixture theory. Principles of development of conservation equations are as follows. First, mixture components may be viewed as isolated subsystems if interactions with other mixture components are properly treated. Second, all properties of the mixture are mathematical consequences of the component properties. Finally, the mean collective mixture behavior is governed by equations similar to those governing the individual components.

$$\nabla \cdot \mathbf{u} = S_m(x, y, z, t) \quad (1)$$

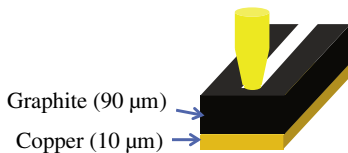


Fig. 2. Anode material.

$$\frac{\partial(\rho u)}{\partial t} + \nabla \cdot (\rho \mathbf{u} \mathbf{u}) = -\frac{\partial p}{\partial x} + \nabla \cdot (\mu \nabla u) + S_u(x, y, z, t) \quad (2)$$

$$\frac{\partial(\rho v)}{\partial t} + \nabla \cdot (\rho \mathbf{u} \mathbf{v}) = -\frac{\partial p}{\partial y} + \nabla \cdot (\mu \nabla v) + S_v(x, y, z, t) \quad (3)$$

$$\frac{\partial(\rho w)}{\partial t} + \nabla \cdot (\rho \mathbf{u} \mathbf{w}) = -\frac{\partial p}{\partial z} + \nabla \cdot (\mu \nabla w) + S_w(x, y, z, t) \quad (4)$$

$$\frac{\partial(\rho \bar{C}_{\text{pl-Cu}} T)}{\partial t} + \mathbf{u} \cdot \nabla (\rho \bar{C}_{\text{pl-Cu}} T) = \nabla \cdot (k \nabla T) + S_E(x, y, z, t) \quad (5)$$

$$\frac{\partial(\rho c)}{\partial t} + \nabla \cdot (\rho \mathbf{u} c) = \nabla \cdot (\rho D \nabla c) + S_c(x, y, z, t) \quad (6)$$

where \mathbf{u} is the liquid velocity vector, x is the Cartesian coordinate along the beam scanning direction, y is the width-wise Cartesian coordinate, z the depth-wise Cartesian coordinate, ρ is the density, μ is the viscosity, p is the pressure, k is the thermal conductivity, $\bar{C}_{\text{pl-Cu}}$ is the average-specific heat of the liquid, and t is the time. S_c , S_m , S_u , S_v , S_w , S_E , and S_c are the source terms for continuity, x-momentum, y-momentum, z-momentum, energy, and species equations. These source terms include boundary conditions for the S/L and L/V interfaces. These source terms are summarized in Table 1. The source terms consist of the boundary conditions of the L/V and S/V interfaces.

2.3. Source terms as boundary conditions of the L/V interface

The first term on the right hand side of the source terms of continuity equation is the boundary condition taking into account evaporation on the L/V interface. To implement vaporization, jump conditions with back pressure are used to take into account discontinuity at the interface caused by the Knudsen layer [21]. The Knudsen layer implemented as jump conditions provides the net mass flux, \dot{m}_{evap}'' , and energy flux \dot{q}_{evap}'' [21,22,25]. The second terms on the right hand side of the source terms of momentum equations, the entire term within parentheses, are boundary conditions for the L/V interface. This model contains both the capillary and thermo-capillary forces, similar to Ki [26]. A third term on the right hand side of the source terms of the energy conservation equation is the boundary condition of the L/V interface.

This term includes energy absorption by multiple reflections, energy losses due to evaporation, and radiation on the L/V interface. $\dot{q}_{L/V}''$ is the spatial laser beam distribution after multiple reflections obtained by using the ray tracing method since total energy transfer from the laser beam to a work piece is significantly

Table 1

Source terms for mass, x-momentum, y-momentum, z-momentum, energy, and species equations.

Equations	Source term
Mass	$S_m(x, y, z, t) = \frac{\dot{m}_{\text{evap}}''}{\rho} \delta(\phi)$
x-momentum	$S_u(x, y, z, t) = -\frac{\mu_1}{K} \frac{\rho}{\rho_1} \mathbf{e}_x \cdot \left(\sigma \mathbf{n} (\nabla \cdot \mathbf{n}) - \nabla_s T \frac{d\sigma}{dT} \right) \delta(\phi)$
y-momentum	$S_v(x, y, z, t) = -\frac{\mu_1}{K} \frac{\rho}{\rho_1} \mathbf{e}_y \cdot \left(\sigma \mathbf{n} (\nabla \cdot \mathbf{n}) - \nabla_s T \frac{d\sigma}{dT} \right) \delta(\phi)$
z-momentum	$S_w(x, y, z, t) = -\frac{\mu_1}{K} \frac{\rho}{\rho_1} \mathbf{e}_z \cdot \left(\sigma \mathbf{n} (\nabla \cdot \mathbf{n}) - \nabla_s T \frac{d\sigma}{dT} \right) \delta(\phi)$
Energy	$S_E(x, y, z, t) = -L \frac{\partial(\rho f_1)}{\partial t} + \frac{\partial(\rho f_2 \Delta \bar{C}_p T)}{\partial t} + [\dot{q}_{L/V}'' - \dot{q}_{\text{evap}}'' - \sigma \epsilon (T^4 - T_\infty^4)] \delta(\phi)$
Species	$S_c(x, y, z, t) = \nabla \cdot [\rho D \nabla (c_1 - c)] - \nabla \cdot [\rho (c_1 - c) \mathbf{u}]$

increased due to the multiple reflections [23]. \dot{q}_{evap}'' is energy loss due to evaporation and $\sigma \epsilon (T^4 - T_\infty^4)$ is energy loss due to radiation. σ and ϵ are Stefan–Boltzmann constant and emissivity, respectively. Note that the simultaneous calculation of the vapor phase and the liquid phase allows for the exclusion of convection heat loss [26].

The formula for the multiple reflections is implemented with ray tracing method [27]. The material properties are smoothed from the liquid to the vapor phase since the L/V interface has significantly different properties [27]. Using ray tracing method, the laser energy is absorbed into the wall at each reflection. At each reflection, the absorption coefficient on the L/V interface is obtained as a summation of the two absorption coefficients, considering the mass fractions, and can be written as

$$A(\alpha) = (1 - f_{C_s})A_{0_Cu}(\cos \alpha)^q + f_{C_s}A_{0_C}(\cos \alpha)^q \quad (7)$$

where α is the incident angle, f_{C_s} is solid mass fraction of graphite, A_{0_Cu} is the absorption coefficient of copper on the flat surface, A_{0_C} is the absorption coefficient of graphite on the flat surface, and q is the characteristic of the material [28]. The calculation of the multiple reflections is terminated when the rays escape the computational domain.

2.4. Source terms as boundary conditions of the S/L interfaces

The boundary conditions of the S/L interface are carefully considered based on the composition changes and mass fractions of the two materials. To incorporate this, this study adopted a method developed by Bennon and Incropera [24]. The first terms on the right hand side of the source terms of momentum equations are the darcian damping force to treat the mushy region as a fine permeable solid matrix. μ_l is the liquid viscosity, and ρ_l is the liquid density. K is the isotropic permeability and is assumed to vary with liquid volume fraction according to the Kozeny–Carman equations [29]:

$$K = K_0 \frac{g_l^3}{(1 - g_l)^2} \quad (8)$$

The first and second terms on the right hand side of the source terms of the energy and species equations are the expression of the mushy zone. These are achieved from Bennon's continuum model [24] by linearizing the phase enthalpies. Derivations are briefly summarized here. Defining the mass fraction, f , and the volume fraction, g , with phases and materials, the velocity, density, thermal conductivity, mass diffusion coefficient, concentration, and enthalpy for the liquid and solid mixtures of the two materials are

$$\mathbf{u} = f_{Cu_s} \mathbf{u}_{Cu_s} + f_{Cu_l} \mathbf{u}_{Cu_l} + f_{C_s} \mathbf{u}_{C_s} \quad (9)$$

$$\rho = g_{Cu_s} \rho_{Cu_s} + g_{Cu_l} \rho_{Cu_l} + g_{C_s} \rho_{C_s} \quad (10)$$

$$k = \left(\frac{g_{Cu_s}}{k_{Cu_s}} + \frac{g_{Cu_l}}{k_{Cu_l}} + \frac{g_{C_s}}{k_{C_s}} \right)^{-1} \quad (11)$$

$$D = f_{Cu_l} D \quad (12)$$

$$c = f_{Cu_l} c_{Cu_l} + f_{Cu_s} c_{Cu_s} \quad (13)$$

$$h = f_{Cu_s} h_{Cu_s} + f_{Cu_l} h_{Cu_l} + f_{C_s} h_{C_s} \quad (14)$$

The relationship between the volume and mass fractions is

$$f_{Cu_s} = \frac{\rho_{Cu_s} g_{Cu_s}}{\rho} \quad (15)$$

$$f_{Cu_l} = \frac{\rho_{Cu_l} g_{Cu_l}}{\rho} \quad (16)$$

$$f_{C_s} = \frac{\rho_{C_s} g_{C_s}}{\rho} \quad (17)$$

The mass and volume fractions must add to unity as follows

$$f_{Cu_s} + f_{C_s} + f_{Cu_l} = 1 \quad (18)$$

$$g_{Cu_s} + g_{Cu_l} + g_{C_s} = 1 \quad (19)$$

and the solid and liquid mass fractions are

$$f_s = f_{Cu_s} + f_{C_s} \quad (20)$$

$$f_l = f_{Cu_l} \quad (21)$$

These defined mixture variables are considered in the continuity equation, momentum equation in x -, y -, and z - directions, energy equations and species equations. The phase enthalpies are obtained as

$$h_{Cu_s} = \int_0^T C_{ps_Cu} dT \quad (22)$$

$$h_{C_s} = \int_0^T C_{ps_C} dT \quad (23)$$

$$h_{Cu_l} = \int_0^{T_m} C_{ps_Cu} dT + L_m + \int_{T_m}^T C_{pl_Cu} dT \quad (24)$$

where T_m is the melting temperature, L_m is the latent heat of fusion, C_{pl_Cu} is the constant-pressure specific heat of the liquid phase of copper, C_{ps_Cu} is the constant-pressure specific heat of the solid phase of copper, and C_{ps_C} is the constant-pressure specific heat of the solid phase of graphite. Furthermore, the average specific heats of solid and liquid (\bar{C}_{ps} and \bar{C}_{pl}) are defined as

$$\bar{C}_{ps_Cu} = \frac{1}{T} \int_0^T C_{ps_Cu} dT \quad (25)$$

$$\bar{C}_{pl_Cu} = \frac{1}{T - T_m} \int_{T_m}^T C_{pl_Cu} dT \quad (26)$$

$$\bar{C}_{ps_C} = \frac{1}{T} \int_0^T C_{ps_C} dT \quad (27)$$

$$h_{C_s} = \bar{C}_{ps,C} T \quad (28)$$

$$h_{Cu_s} = \bar{C}_{ps,Cu} T \quad (29)$$

$$\begin{aligned} h_{Cu_l} &= \bar{C}_{ps,Cu} T_m + L_m + \bar{C}_{pl,Cu} (T - T_m) \\ &= \bar{C}_{pl,Cu} T + (\bar{C}_{ps,Cu} - \bar{C}_{pl,Cu}) T_m + L_m = \bar{C}_{pl,Cu} T + L \end{aligned} \quad (30)$$

where $L = (\bar{C}_{ps,Cu} - \bar{C}_{pl,Cu}) T_m + L_m$. By using the defined mixture variables, the boundary conditions for the S/L interface can be calculated by substituting Eqs. (28)–(30) into Eq. (14).

$$h = (f_{C_s} \bar{C}_{ps,C} + f_{Cu_s} \bar{C}_{ps,Cu} + f_{Cu_l} \bar{C}_{pl,Cu}) T + f_{Cu_l} L = \bar{C}_p T + f_{Cu_l} L \quad (31)$$

where \bar{C}_p is the average mixture specific heat, defined as

$$\bar{C}_p = f_{C_s} \bar{C}_{ps,C} + f_{Cu_s} \bar{C}_{ps,Cu} + f_{Cu_l} \bar{C}_{pl,Cu} \quad (32)$$

and can be written as

$$\bar{C}_p = \bar{C}_{pl,Cu} - f_s \Delta \bar{C}_p \quad (33)$$

$$\Delta \bar{C}_p = \frac{f_{Cu_s}}{f_s} (\bar{C}_{pl,Cu} - \bar{C}_{ps,Cu}) + \frac{f_{C_s}}{f_s} (\bar{C}_{pl,Cu} - \bar{C}_{ps,C}) \quad (34)$$

Now, the first and second terms on the right hand side of the source terms of the energy equation can be obtained by substituting the above relations, as described by Ki [30]. At this point, the mass fractions have to be obtained and updated for each numerical iteration. The phase diagram can provide these values. Since the currently available phase diagram provides limited information, the rest of the phase diagram is extrapolated to the sublimation temperature of pure graphite using piecewise continuous functions as shown in Fig. 3. The solid and liquid fractions can be obtained by the lever rule (Fig. 3).

A boundary condition for the S/L interface of the composition equation can be written as

$$c_0 \delta(\psi) = 1 \quad (35)$$

where c_0 is initial composition of copper and ψ indicates the S/L interface. Considering the boundary condition during the computation on the S/L interface, the concentration of copper into graphite can be fully included in this mathematical model.

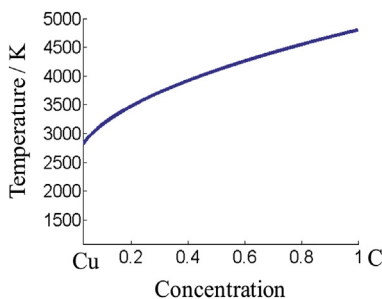


Fig. 3. Extended C–Cu phase diagram.

2.5. Level set equation for the L/V interface tracking

During laser cutting, the L/V interface is continuously changing due to complex physical phenomena at the interface such as evaporation, convective flow, multiple reflections, energy absorption, energy loss, and significantly different properties between liquid and vapor. This section describes the implementation of these interfacial phenomena into the proposed model. A key factor in the investigation of the interface shape and the process physics is the tracking of the free surface. Osher and Sethian [31] developed the level set method. This method has increasingly been used for many complex problems due to its easy implementation, straightforward concept, ability to handle surface merging and separation automatically, and easy achievements of geometric qualities, such as the surface normal and the curvature on the surface.

The L/V interface, which is the surface of interest, is set as the zero iso-surface or $\phi(\mathbf{x}, t)$, to implement the level set method. By equating this zero iso-surface with zero and taking the material derivative, we can get the level set equation in terms of a hyperbolic partial differential equation.

$$\frac{\partial \phi}{\partial t} + F |\nabla \phi| = 0 \quad (36)$$

where F is the speed function. The detail derivation of this equation can be found in Ref. [32].

During the laser cutting process, the L/V interface in the level set equation, i.e. $\phi = 0$, is evolved on the basis of the speed function, which is composed of vaporization and fluid flow. By solving the proposed momentum equation, the fluid flow can be obtained. To implement vaporization into the speed function, jump conditions with back pressure are used to take into account a thin discontinuity of the order of a molecular mean free path thickness at the interface. Hence, a final form of the speed function is

$$F = F_{\text{evap}} + \mathbf{u} \cdot \mathbf{n} \quad (37)$$

where \mathbf{u} is the liquid velocity vector, \mathbf{n} is the normal vector, and F_{evap} is the vaporizing mass flux, which is assumed to be perpendicular to the L/V interface and obtained by the Mott-Smith-type solution [21,22,25].

3. Experiments

Experimental investigation is designed with an IPG single mode CW fiber laser (model: YLR-500SM) with the diameter of 11 μm and the wavelength of 1.070 μm . Its maximum laser power is 500 W. The laser beam is delivered by a fiber with a 10 μm core-fiber diameter and collimated to a beam diameter of 13 mm. This fiber-delivered laser beam is deflected and moved by a 2D galvo-scanner, made by Scanlab (model: SK1020K), at high dynamic speeds with maximum speeds up to 5 m s⁻¹. The 2D galvo-scanner is connected to an 80 mm F-theta lens, which keeps the scanning image field flat within a 35 × 35 mm square field size. The laser beam is measured using FocusMonitor, manufactured by Primes. The measured spot is symmetrical and has closely Gaussian energy distribution as shown in Fig. 4. At the focus position the measured value of spot size is approximately 11 μm . The Rayleigh length of 70 μm and M^2 value (86%) of 1.3 are obtained from this measurement.

Fig. 5 shows the schematic of the experimental set up. Cutting is performed as the laser beam is moving across a stationary anode surface using a high speed galvo-scanner. A vacuum fixture is used to hold anodes and prevent any movement during the entire cutting process. A narrow groove, which is less than 0.5 mm, was placed in the top plate of the fixture where the cutting takes place.

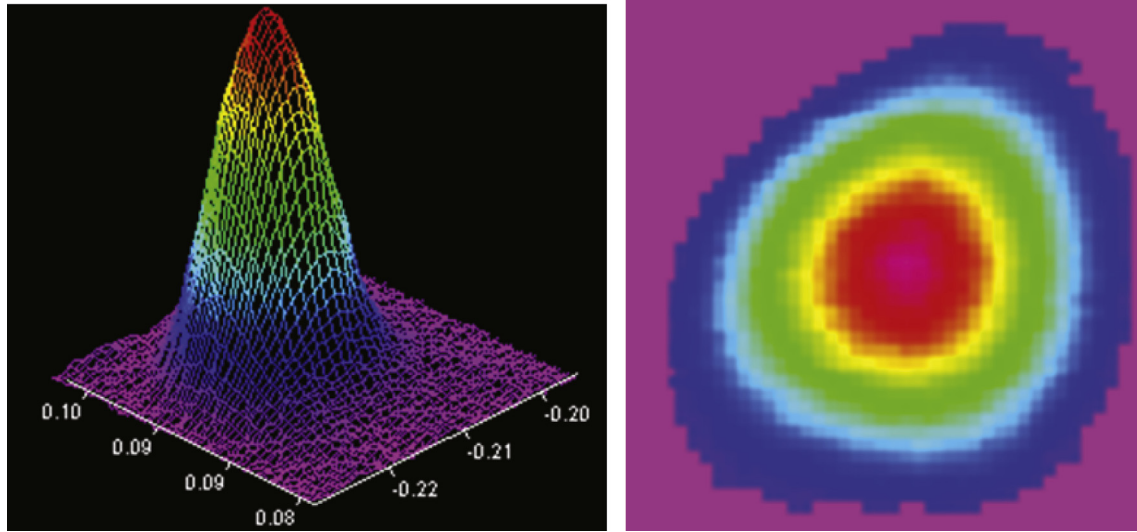


Fig. 4. Measured laser beam shape.

This prevents any attachments of melt that moves out of cut kerf to the fixture plate. The fixture is mounted on the horizontal plane of a CNC motion system and the 2D galvo-scanner is mounted on its vertical axis. Using this precise 3 axis positioning system, the scanner was aligned with the fixture and placed at the correct vertical distance from the anode. There is no process gas applied during cutting. Cutting is performed in a clean and dust free environment with suitable fume exhaust systems. The single side-coated anode is used as seen in Fig. 2. The anode is placed on the fixture as graphite faces upward and the laser beam irradiates on the graphite surface. Thickness of graphite and copper are 90 μm and 10 μm , respectively. Average particle size of graphite is 20.36 μm . The density of the graphite part of the coated anode is 120 g m^{-3} . Graphite is composed of active graphite powder (92.5%), CMC (1.5%), SBR liquid (2.5%), and Conductive (3.5%).

4. Results and discussions

4.1. Simulation preparations and solution schemes

A CW Gaussian laser beam is used and scanned in the positive x direction. A focused beam diameter is 11 μm . It is assumed that the beam profile has no z dependency.

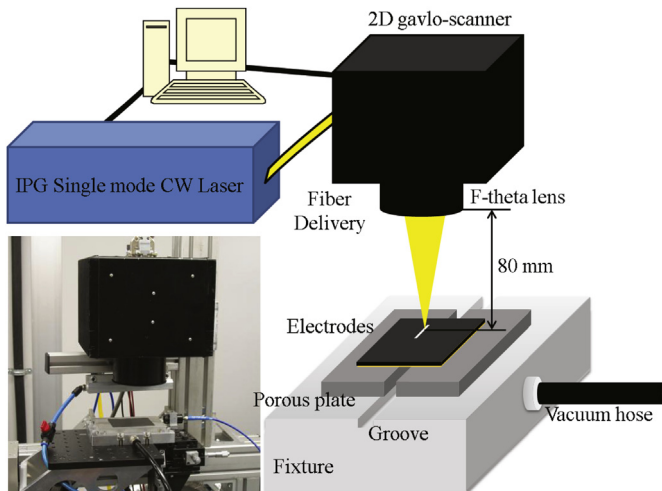


Fig. 5. Experimental set up.

$$I(r) = I_0 \exp\left(-\frac{2r^2}{R_b^2}\right) \quad (38)$$

where R_b is the beam radius and I_0 is the centerline laser intensity. The laser power and scanning speed chosen for this study are 450 W and 5 m s^{-1} , respectively. The computational domain of the simulation is 55 $\mu\text{m} \times 30 \mu\text{m} \times 130 \mu\text{m}$. Non-uniform mesh is used to save

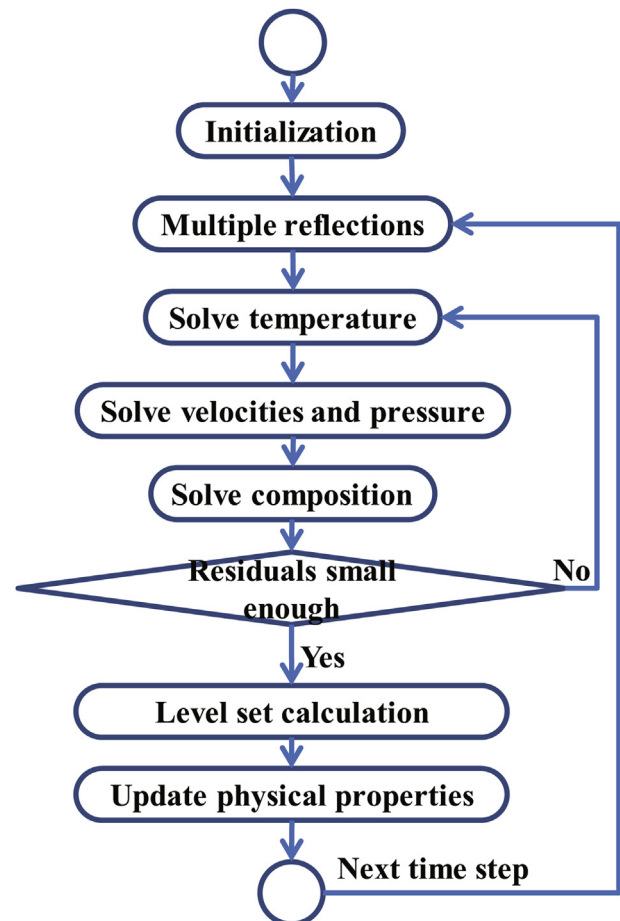


Fig. 6. Simulation flow diagram.

Table 2
Material properties of copper.

Property	Value
Melting temperature	1357.77 (K)
Normal boiling temperature	2835.15 (K)
Critical point temperature	8280 (K)
Liquid density	7920 (kg m ⁻³)
Solid density	8960 (kg m ⁻³)
Kinematic viscosity [36]	3.50E – 07 (m ² s ⁻¹)
Surface tension [37]	1.257 – 0.0002(T – 1356) (N m ⁻¹)
Latent heat of vaporization	5.23E + 06 (J kg ⁻¹)
Latent heat of fusion	2.05E + 05 (J kg ⁻¹)
Solid thermal conductivity [38]	317 (W m ⁻¹ K ⁻¹)
Liquid thermal conductivity [38]	157 (W m ⁻¹ K ⁻¹)
Liquid constant-pressure specific heat	571.6218 (J kg ⁻¹ K ⁻¹)
Solid constant-pressure specific heat [39]	385 (J kg ⁻¹ K ⁻¹)
Liquid thermal diffusivity	3.62E – 05 (m ² s ⁻¹)
Solid thermal diffusivity	7.63E – 05 (m ² s ⁻¹)
Laser absorptivity for flat surface	0.05

computational time. The smallest discrete mesh distance is chosen as 0.6 μm . A staggered grid is utilized to attain the physically proper pressure field [33]. One side graphite-coated copper is chosen as the substrate material, where the thickness of the anode is 100 μm . Graphite of 90 μm and copper of 10 μm are placed as the top and bottom layers of the anode, respectively. The properties of these materials are shown in Tables 2 and 3. An implicit finite difference method is used for the discretization of the governing equations. To solve the matrix equation and coupled pressure–velocity fields on the staggered grid system, the conjugated Gradient Stabilized (CGSTAB) method and Semi-Implicit Method for Pressure-Linked Equation-Consistent (SIMPLEC) are adopted, respectively. In addition, a second-order space convex scheme [34] is used to discretize the spatial derivative of the level set equation. Finally, the value of c for all of the material properties is taken 0.8 and $7 \times \min(\Delta z)$ is chosen for ε . Δz is the shortest length of the smallest mesh.

A flow diagram of the solution procedure in one time step is shown in Fig. 6. First, simulation parameters and material properties are assigned. In addition, the jump conditions for the Knudsen layer are tabulated as an initialization step. Second, the multiple reflections are executed. Third, the temperature, velocities, and concentration of copper are solved sequentially in an inner loop with coupled solutions until the coupled solutions satisfy computational residuals. A maximum iteration is set to prevent unnecessary computations due to slow convergence, even if the residual values are not satisfied. Fourth, the level set equation is calculated with the obtained values of evaporation and convection, which are main sources of interface deformation. Finally, the mixture properties are updated with a given liquid mass fraction through the phase diagram. This procedure is repeated until it satisfies the designated computation time.

4.2. Characteristics of the anode laser cutting

In the following sections, the top layer (90 μm) is called the graphite region; the bottom layer (10 μm) is called the copper region.

Table 3
Material properties of graphite.

Property	Value
Sublimation temperature [40]	4800 (K)
Critical point temperature [41]	7811 (K)
Solid density [42]	1730 (kg m ⁻³)
Latent heat of sublimation [42]	5.98E + 07 (J kg ⁻¹)
Solid thermal conductivity [42]	18.1 (W m ⁻¹ K ⁻¹)
Solid constant-pressure specific heat [42]	2092.48 (J kg ⁻¹ K ⁻¹)
Solid thermal diffusivity [42]	5.00E – 06 (m ² s ⁻¹)
Laser absorptivity for flat surface	0.81

Penetration depth, width, and absorptivity with evolution of time are shown in Fig. 7. A deep penetration hole reaches a material interface between graphite and copper at 0.1646 μs . Around this material interface, several interesting overall behaviors are observed. The slope of the depth increase of the deep penetration hole changes over time. Before the deep penetration hole reaches the material interface, its slope of the depth increase is 722.16 m s⁻¹. Once the depth of the deep penetration hole reaches the material interface, the slope decreases to 288.00 m s⁻¹. The width increases gradually and it becomes 31.196 μm when the deep penetration hole reaches the material interface. This gradual increase of width is possible since the width is measured on the top surface of the anode. At the beginning of the simulation, the absorptivity is 0.81, which is the absorption coefficient of graphite as a flat substrate. The maximum absorptivity is 0.9588 at which point the deep penetration hole reaches the material interface. After obtaining the maximum value at 0.1646 μs , absorptivity starts to decrease gradually with fluctuation and then it increases again before it has completed thorough cutting.

Characteristics of penetration depth and absorptivity change significantly at the point where the deep penetration hole reaches the material interface. These observations are closely related to each other and due mainly to the composition change at the material interface. An absorption coefficient changes its value depending on the mass fraction on the surface, since the absorption coefficient is obtained by a summation of the two absorption coefficients of the graphite and copper with mass fractions as described in Eq. (8). Increasing the copper concentration around the material interface contributes to decreasing the absorption coefficient of the mushy zone so that absorptivity decreases. The

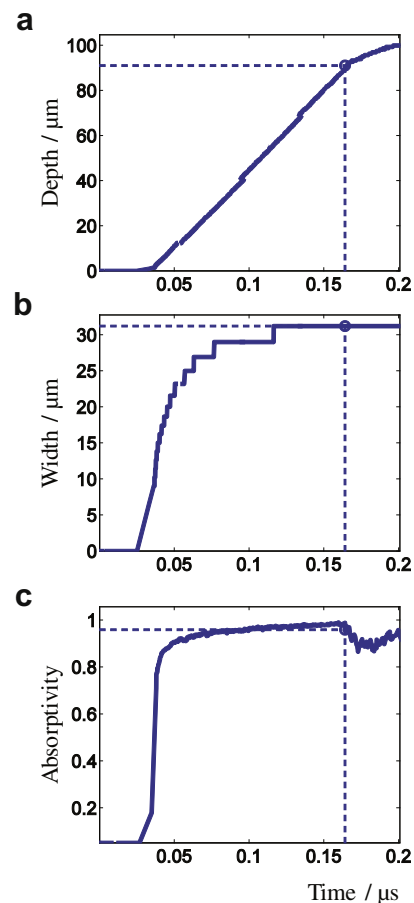


Fig. 7. Penetration depth (a), width (b), and absorptivity (c) with time.

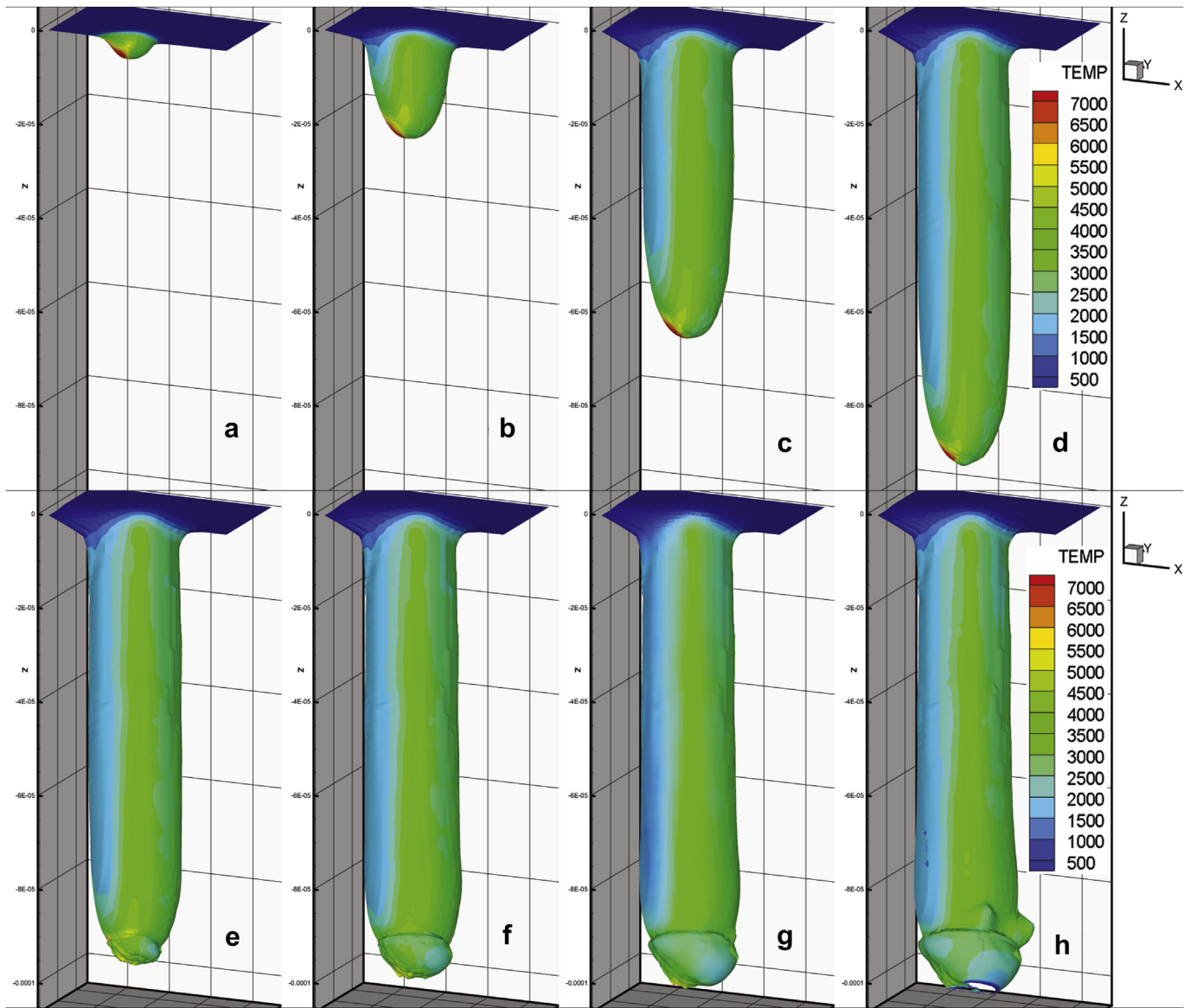


Fig. 8. Temperature distribution and melt pool geometry of anode (laser power: 450 W, scanning speed: 5000 mm s⁻¹) at (a) 0.043 μ s, (b) 0.066 μ s, (c) 0.126 μ s, (d) 0.164 μ s, (e) 0.172 μ s, (f) 0.183 μ s, (g) 0.192 μ s, (h) 0.200 μ s.

decrease of absorptivity provides less energy absorption on the L/V interface. Therefore, the rate of depth increases changes.

4.3. Temperature distribution and melt pool geometry

Temperature distribution and melt pool geometry are shown in Fig. 8. At the beginning of the simulation, the deep penetration hole shows a very smooth and clean surface as seen in Fig. 8 (a)–(c). The surface shows clearly the characteristic of the laser cutting of graphite, which was investigated in the study of laser cutting on an active electrode material [35]. No liquid phase exists for graphite since it sublimates. Hence, the resulting surface is smooth and clean. In addition, high temperatures are observed in the front and back side of the L/V interface due to multiple reflections. When the deep penetration hole reaches the material interface, a melt pool starts to form as seen in Fig. 8 (d). After this initial melt pool formation, the melt pool develops and shows the two-level surface, two-step-like shape, as shown in Fig. 8 (g). This two-level surface can be explained by the different material properties between

graphite and copper. While no surface changes in the graphite region due to its sublimation property, melt pool flow observed in the copper region changes the geometry of the bottom part of the deep penetration hole. Therefore, two-level surfaces form.

Penetrations on the side and front of the deep penetration hole at the moment of full penetration are observed as shown in Fig. 8 (h). The movement of the liquid copper causes the fluctuation motion of the deep penetration hole and creates an uneven melt pool shape in the copper region. This uneven shape reflects a laser beam toward the graphite region and graphite sublimates due to the absorption of reflected laser energy. Hence, the reflected laser beam forms the front and side penetrations and changes the melt pool geometry dramatically around the material interface.

4.4. Copper composition distribution and melt pool flow

Figs. 9 and 10 show copper composition distribution and melt pool flow, respectively. No copper composition and melt pool flow are shown in Figs. 9 (a)–(c) and 10 (a)–(c) since the deep

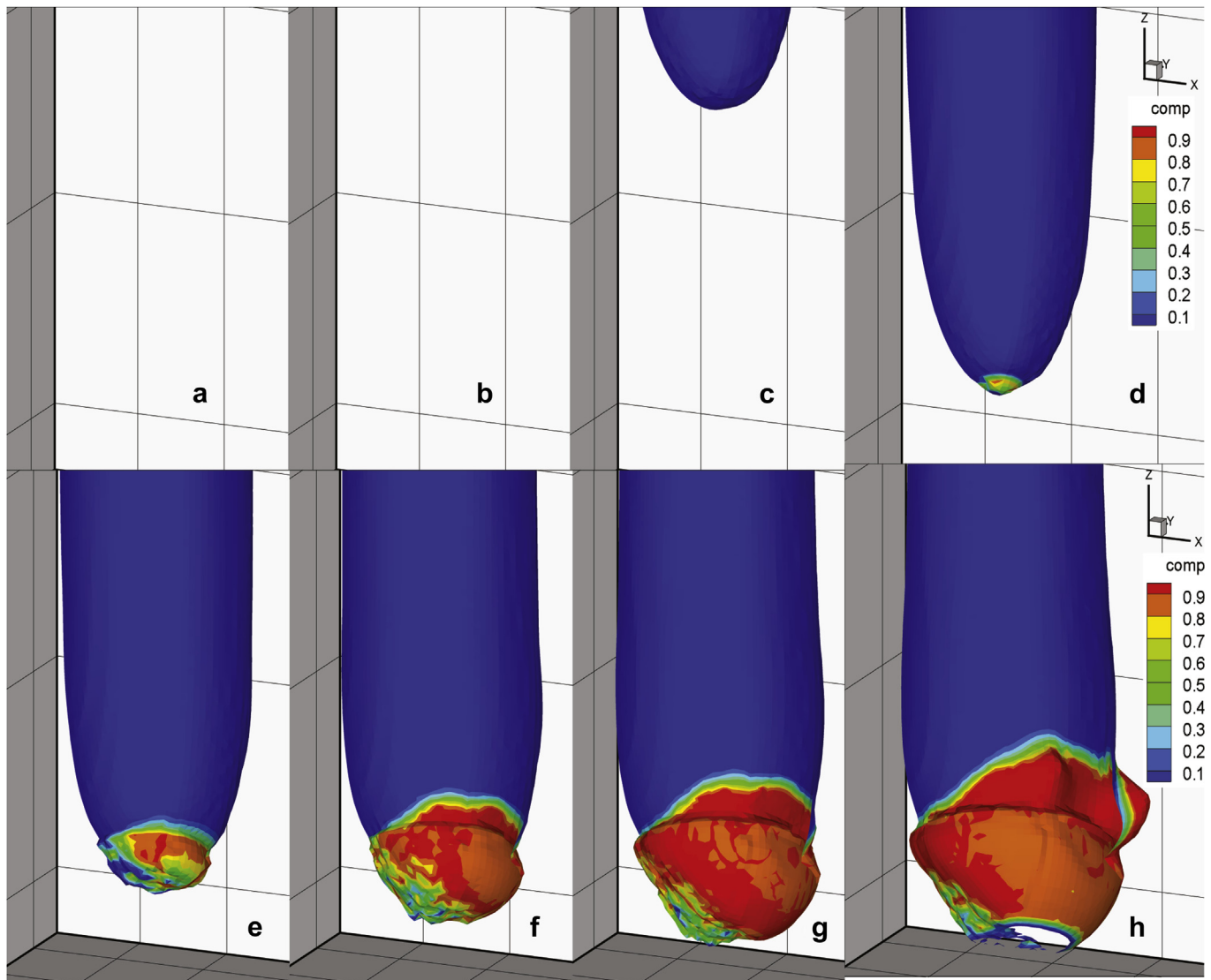


Fig. 9. Copper composition distribution (laser power: 450 W, scanning speed: 5000 mm s⁻¹) at (a) 0.043 μs, (b) 0.066 μs, (c) 0.126 μs, (d) 0.164 μs, (e) 0.172 μs, (f) 0.183 μs, (g) 0.192 μs, (h) 0.200 μs.

penetration hole forms in the graphite region. When the deep penetration hole reaches the material interface, energy transfers from the graphite surface to the solid copper. The copper increases its temperature to the melting point so that the copper starts to melt and the melt pool forms. Next, the copper concentration starts to increase at the material interface, as seen in Figs. 9 (d) and 10 (d). At the beginning of the mass transfer, higher values of the copper concentration are observed on the front and side walls of the deep penetration hole as shown in Fig. 9 (e). In Fig. 9 (f)–(h), as the deep penetration hole is becoming deeper, the copper concentration is distributed more uniformly on the copper region; copper concentration on the graphite region increases around the deformed graphite surface. However, the back side of the deep penetration hole in the copper region shows less copper concentration. The front melt pool provides stronger melt pool flow, as seen in Fig. 10 (e)–(h). Furthermore, melt pool flow is observed on the graphite region due to the existence of the liquid copper. When a full penetration occurs, as shown in Fig. 9 (h), the copper concentration is relatively low around the bottom of the penetrated hole. Stronger flow is observed around the deformed graphite surface, as shown in Fig. 10 (h).

4.5. Comparison between simulation and experiments

The top view of a laser cut anode is shown in Fig. 11 (a). A laser irradiates the graphite surface as shown in Fig. 2. Kerf widths on the top and bottom layers are 97.60 μm and 27.90 μm, respectively. Luetke et al. [19] defined the clearance width of the metal foil of anodes for lithium-ion batteries, which is the ablation width of the upper coating. This study also observes the clearance width of 29.10 μm. These experimental results clearly show the two-level surface on the material interface, which is also observed in the simulation result. The kerf width obtained by simulation is 31.19 μm and shown in Fig. 11 with a dashed line. The simulation result overestimates the kerf width of the bottom layer by 7.18%, which is in good agreement with the experimental measurement. However, the kerf width of the top layer shows discrepancy compared to the kerf width obtained by the simulation. The discrepancy of the kerf width, which is characterized by the clearance width, can be explained from the computational analysis. The fluctuation motion of the deep penetration hole due to the liquid flow of copper creates uneven melt pool shape at the tip of the deep penetration hole. The

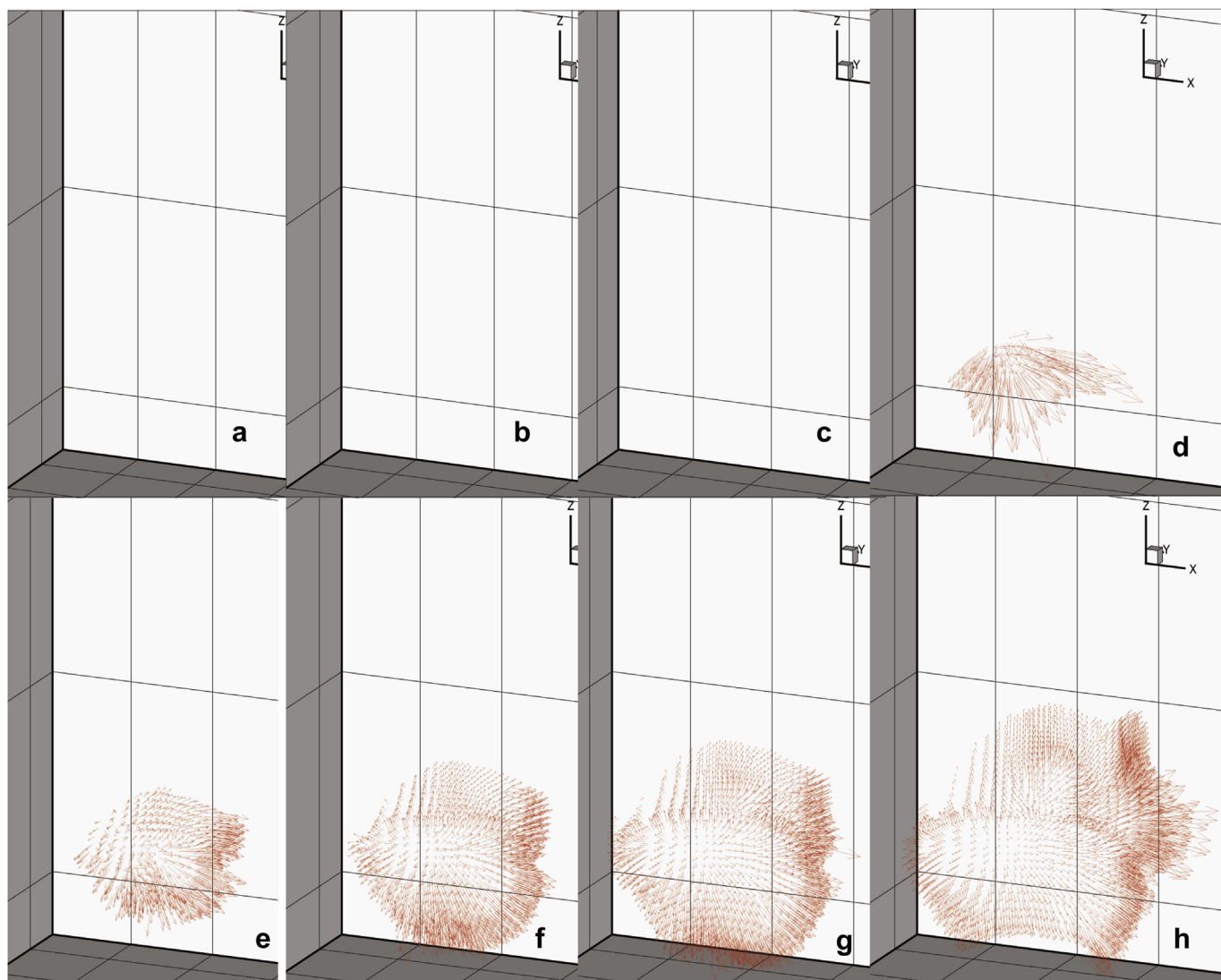


Fig. 10. Melt pool flow of anode (laser power: 450 W, scanning speed: 5000 mm s^{-1}) at (a) $0.043 \mu\text{s}$, (b) $0.066 \mu\text{s}$, (c) $0.126 \mu\text{s}$, (d) $0.164 \mu\text{s}$, (e) $0.172 \mu\text{s}$, (f) $0.183 \mu\text{s}$, (g) $0.192 \mu\text{s}$, (h) $0.200 \mu\text{s}$.

reflected laser beam toward the graphite region from the uneven melt pool shape sublimates graphite. Hence, the kerf widths of the graphite region and copper region are different. The side view of the laser cut anode is shown in Fig. 11 (b). It shows good quality of cut surface. No delamination, edge banding, burrs, or micro-size attachments on the material interface are observed. At the bottom of the anode, debris caused by re-solidification is observed. Copper concentrations, which are obtained by both the simulation and experiment, are analyzed along the perpendicular line as shown in Fig. 12 and its values are plotted in Fig. 13. The copper concentration of the experimentally obtained anode sample was obtained through Energy-Dispersive X-ray spectroscopy (EDX) analysis.

From the top surface to the depth of $71.31 \mu\text{m}$, the experimentally measured copper concentration is lower than 10% and shows no trend. The copper concentration increases significantly from the depth of $71.31 \mu\text{m}$ to $82.55 \mu\text{m}$ and reaches its value of 99.68% at the depth of $82.55 \mu\text{m}$. As it becomes deeper, the copper concentration gradually decreases from the 99.68% to 16.12%, from the depth of $82.55 \mu\text{m}$ to the material interface, and then it increases again and becomes 100% copper concentration at the

depth of $100 \mu\text{m}$. For the computationally obtained copper concentration, there is no copper concentration observed from the top surface to the depth of $73.96 \mu\text{m}$. From the depth of $73.96 \mu\text{m}$ to $74.56 \mu\text{m}$, a small amount of copper concentration is found. The copper concentration increases significantly and becomes 100% at the depth of $84.73 \mu\text{m}$. The copper concentration stays at 100% until at the depth of $89.52 \mu\text{m}$ and then decreases up to 78.02% at the depth of $99.10 \mu\text{m}$. Both experimentally and computationally obtained copper concentrations share three characteristics. First, the copper concentration starts to increase its value at least $10 \mu\text{m}$ above the material interface. Second, it increases very sharply up to 100% copper concentration after its initial increase. Third, the copper concentration decreases once 100% copper concentration is achieved. The reason of the 99–100% copper concentration at about $10 \mu\text{m}$ above the material interface is the direction of liquid copper as we see in Fig. 10. The thorough penetration may affect the decrease of the copper concentration near the material interface. In addition, the flow direction removes liquid copper from the bottom of the deep penetration hole to the outward direction. This also explains the 99–100% copper concentration at about $10 \mu\text{m}$ above the material interface.

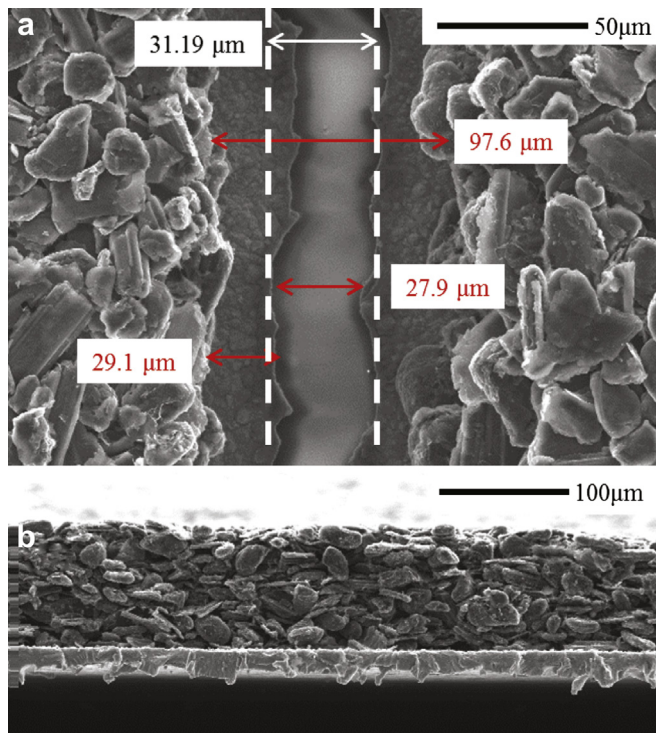


Fig. 11. Top view (a) and side view (b) of laser cut anode.

Although both computational and experimental results share similar trends, there is a discrepancy in terms of kerf widths and the copper concentration. The discrepancy may be caused by three main reasons. First, graphite is mixed with additives and binders during the graphite coating process. Hence, its material properties could be different from the material properties of pure graphite, adapted in this simulation. Second, the extended copper and graphite binary diagram may give rise to this discrepancy. The liquid fraction can be overestimated since the binary diagram is extended. Finally, the simulation does not take into account the

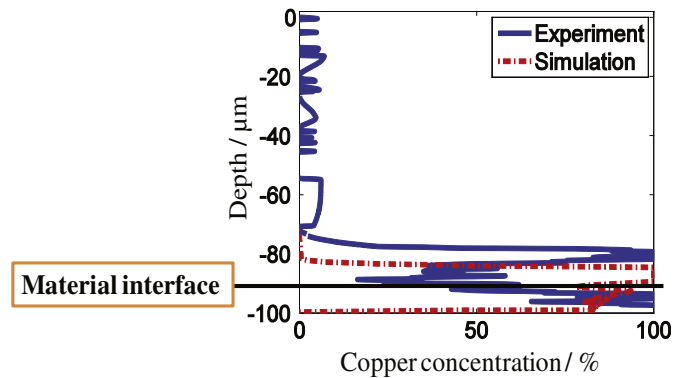


Fig. 13. Comparison of the copper composition between experiment and simulation.

reaction with oxygen, or the air suction to hold the sample surface flat.

As mentioned above, the properties of the coated graphite layer are different from those of pure graphite. The graphite layer of experimental electrode probably has a lower solid density, a higher porosity and a lower thermal conductivity. These differences may affect entire simulation results. First of all, the kerf width and the slope of depth penetration may be decreased since the coated graphite layer has a lower solid density, a higher porosity and a lower thermal conductivity. Furthermore, flow speed and pattern of the liquid copper could be changed since the geometry of the first layer highly influence the transport phenomena of the liquid copper during the laser material interaction.

The simulation analysis in this study found strong outward liquid flow at the front of the deep penetration and composition changes on the graphite region. The strong outward flow of liquid copper gives rise to composition change and sharp edge formation on the cut surface. The composition change on the material interface may result in non-uniform electrochemical reactions and higher electrical stress, which can lead to significant heat generation and possible thermal runaway during the use of the lithium-ion battery cell. In addition, the sharp edge could penetrate the separator so that an internal short circuit occurs.

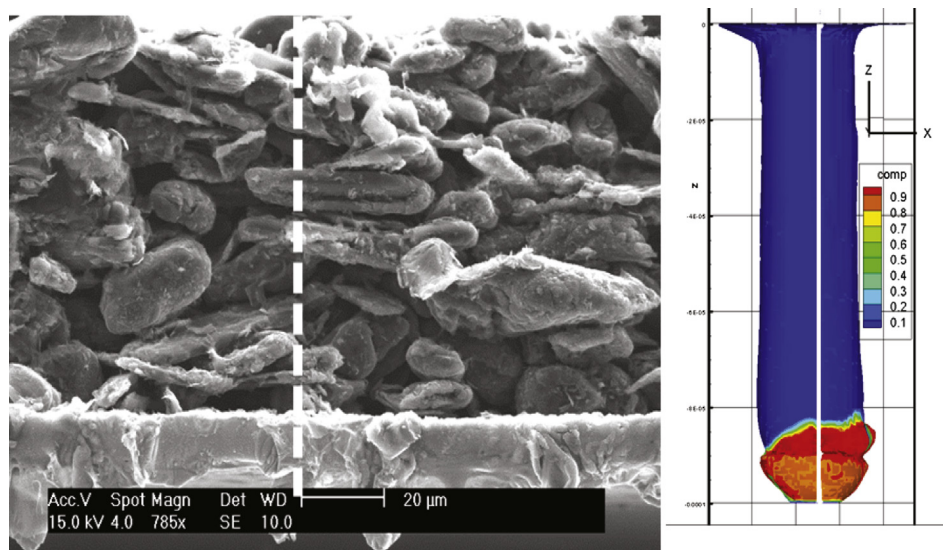


Fig. 12. Copper composition variation along the line both for experimental sample (a) and simulation (b).

5. Conclusions

Laser cutting allows an improved quality of cut surface and cutting speed during lithium-ion battery manufacturing processes. The advantages of laser cutting can be maximized by understanding the underlying physics during the laser cutting of electrodes for lithium-ion batteries. To understand the underlying physics, a mathematical model of three-dimensional self-consistent laser cutting of an anode for lithium-ion batteries is developed including multiple physical phenomena such as heat transfer, composition changes, fluid flow, recoil pressure, capillary and thermo-capillary forces, multiple reflections, and Knudsen layer.

The analysis of simulation results presents the characteristics of the laser cutting of anode for lithium-ion batteries. Characteristics of penetration depth and absorptivity change significantly at the point where the deep penetration hole reaches the material interface due mainly to the composition change at the material interface. Furthermore, temperature distribution, melt pool geometry, melt pool flow, and composition distribution are examined.

At the beginning of the simulation, the L/V interface shows a smooth and clean surface due to the sublimation characteristics of graphite. When the deep penetration hole reaches the material interface, a melt pool starts to form, develops and results in a two-level surface due mainly to the sublimation property of graphite and the melt pool flow of liquid copper. In addition, higher values of the copper concentration are observed around the material interface. When the deep penetration hole is becoming deeper, the copper concentration is distributed more uniformly and the front melt pool provides strong melt pool flow in the copper region. In the graphite region, the copper concentration increases around the deformed graphite surface and melt pool flow is observed due to the existence of the liquid copper. Penetrations on the side and front of the deep penetration hole at the moment of full penetration are observed since uneven melt pool shape in the copper region reflects the laser beam to the graphite region. The copper concentration is relatively low around the bottom of the penetrated hole. Stronger flow is observed around the deformed graphite surface.

The cut surface, kerf width, and copper composition of the experimentally obtained sample are measured by SEM and EDX analyses. A good cut surface is observed and kerf widths show a discrepancy with simulation results. The discrepancy may be caused by the properties of the graphite sample used for the experiments, the extended copper and graphite binary diagram in the simulation, or the lack of oxygen reaction and air suction included in the simulation. In spite of these discrepancies, both experimentally and computationally obtained copper concentrations share key characteristics. The copper concentration starts to increase its value at least 10 μm above the material interface and increases very sharply up to 100% copper concentration after its initial increase. In addition, the copper concentration decreases once 100% copper concentration is achieved.

The proposed mathematical model of laser cutting of an anode for lithium-ion batteries can be utilized to predict and prevent the defects or thermal stress observed during the laser cutting process by analyzing the melt pool and temperature distribution. Furthermore, laser parameters can be optimized through this model to minimize the mass transfer of copper into the graphite region.

Acknowledgments

This effort was supported by the University of Michigan – Fraunhofer Alternative Energy Technologies for Transportation Program (AETT Program). The authors appreciate the support from our sponsors.

Nomenclature

Physical constant

R	gas constant, $8.314 \text{ J K}^{-1} \text{ mol}^{-1}$
σ	Stefan–Boltzmann constant, $5.67 \times 10^{-8} \text{ W m}^{-2} \text{ K}^{-4}$

Symbols

α	incident angle, $^\circ$
$A_{0,\text{Cu}}$	absorption coefficient of copper
$A_{0,\text{C}}$	absorption coefficient of graphite
C_{pl}	liquid constant-pressure specific heat, $\text{J kg}^{-1} \text{ K}^{-1}$
C_{ps}	solid constant-pressure specific heat, $\text{J kg}^{-1} \text{ K}^{-1}$
\bar{C}_{p}	average constant-pressure mixture specific heat, $\text{J kg}^{-1} \text{ K}^{-1}$
\bar{C}_{pl}	average constant-pressure specific heat of liquid, $\text{J kg}^{-1} \text{ K}^{-1}$
\bar{C}_{ps}	average constant-pressure specific heat of solid, $\text{J kg}^{-1} \text{ K}^{-1}$
δ	delta function
$\mathbf{e}_x, \mathbf{e}_y, \mathbf{e}_z$	unit vectors in x, y, z directions, respectively
ε	emissivity
f_{l}	liquid mass fraction
f_{s}	solid mass fraction
g_{l}	liquid volume fraction
g_{s}	solid volume fraction
F	force function, m s^{-1}
F_{evap}	speed function of the L/V interface due to evaporation, m s^{-1}
h	enthalpy, J kg^{-1}
h_{l}	liquid enthalpy, J kg^{-1}
h_{s}	solid enthalpy, J kg^{-1}
$H_{\varepsilon, c(\phi)}$	smoothing function
i	incoming ray
k	thermal conductivity, $\text{W m}^{-1} \text{ K}^{-1}$
k_{l}	liquid thermal conductivity, $\text{W m}^{-1} \text{ K}^{-1}$
k_{s}	solid thermal conductivity, $\text{W m}^{-1} \text{ K}^{-1}$
κ	curvature
L_{m}	latent heat of fusion, J kg^{-1}
L_{v}	latent heat of vaporization, J kg^{-1}
μ	viscosity, $\text{m}^2 \text{ s}^{-1}$
μ_{vap}	vapor viscosity, $\text{m}^2 \text{ s}^{-1}$
μ_{liq}	liquid viscosity, $\text{m}^2 \text{ s}^{-1}$
\dot{m}''	net mass loss due to evaporation per area, $\text{kg s}^{-1} \text{ m}^{-2}$
\mathbf{n}	normal vector
p	pressure, Pa
ρ	density, kg m^{-3}
ρ_{l}	liquid density, kg m^{-3}
ρ_{s}	solid density, kg m^{-3}
\dot{q}''	the actual net energy influx at the Liquid–Vapor interface per area, $\text{J s}^{-1} \text{ m}^{-2}$
$\dot{q}''_{\text{L/V}}$	the spatial laser beam distribution after multiple reflections per area, $\text{J s}^{-1} \text{ m}^{-2}$
\dot{q}''_{evap}	energy loss due to evaporation per area, $\text{J s}^{-1} \text{ m}^{-2}$
R_{v}	specific gas constant, $\text{J kg}^{-1} \text{ K}^{-1}$
r	reflected ray
σ	surface tension, N m^{-1}
t	time, s
T	temperature, K
T_{s}	temperature at surface, K
T_{m}	melting temperature, K
T_{b}	boiling temperature, K
T_{v}	temperature at vapor, K
\mathbf{u}	fluid velocity vector, m s^{-1}
u_{v}	velocity of vapor, m s^{-1}

x	spatial vector
ϕ	level set function

Abbreviations

L/V	Liquid–Vapor interface
S/L	Solid–Liquid interface
HEV	Hybrid Electric Vehicle
PHEV	Plug-in Hybrid Electric Vehicle
EV	Electric Vehicle

References

- [1] M. Alamgir, A.M. Sastry, SAE Convergence, Detroit, MI, 2008.
- [2] M. Winter, R.J. Brodd, Chem. Rev. 104 (2004) 4245–4269.
- [3] M. Park, X. Zhang, M. Chung, G.B. Less, A.M. Sastry, J. Power Sources 195 (2010) 7904–7929.
- [4] M. Broussely, P. Biensan, B. Simon, Electrochim. Acta 45 (1999) 3–22.
- [5] Q. Wang, W. Zhang, Z. Yang, S. Weng, Z. Jin, J. Power Sources 196 (2011) 10176–10182.
- [6] T. Muraliganth, A.V. Murugan, A. Manthiram, J. Mater. Chem. 18 (2008) 5661–5668.
- [7] A.V. Murugan, T. Muraliganth, A. Manthiram, J. Phys. Chem. C 112 (2008) 14665–14671.
- [8] R. Amin, P. Balaya, J. Maier, Electrochem. Solid State Lett. 10 (2007) A13–A16.
- [9] H. Kim, J. Cho, Nano Lett. 8 (2008) 3688–3691.
- [10] C.C. Nguyen, S.-W. Song, Electrochem. Commun. 12 (2010) 1593–1595.
- [11] H. Guo, H. Zhao, C. Yin, W. Qiu, J. Alloys Compd. 426 (2006) 277–280.
- [12] M.N. Obrovac, L. Christensen, Electrochem. Solid State Lett. 7 (2004) A93–A96.
- [13] T. Zhang, J. Gao, L.J. Fu, L.C. Yang, Y.P. Wu, H.Q. Wu, J. Mater. Chem. 17 (2007) 1321–1325.
- [14] H.J. Herfurth, R. Patwa, H. Pantsar, S. Heinemann, G. Newaz, in: Proceedings of the ICALEO, Temecula, CA, USA, 2008.
- [15] H.J. Herfurth, R. Patwa, H. Pantsar, in: Proceedings of the LPM, Germany, 2010.
- [16] R. Patwa, H.J. Herfurth, H. Pantsar, S. Heinemann, J. Mazumder, D. Lee, in: Proceedings of the ICALEO, Anaheim, CA, 2010.
- [17] Woodbank Communications, http://www.mpoweruk.com/battery_manufacturing.htm.
- [18] W.M. Steen, J. Mazumder. SpringerLink (Online service), Springer-Verlag London, London, 2010.
- [19] M. Luetke, V. Franke, A. Techel, T. Himmer, U. Klotzbach, A. Wetzig, E. Beyer, Phys. Procedia 12 (2011) 286–291.
- [20] D. Lee, J. Mazumder, in: Proceedings of the ICALEO, Laser Institute of America, Anaheim, California, 2010.
- [21] C.J. Knight, AIAA J. 17 (1979) 519–523.
- [22] T. Ytrehus, S. Ostmo, Int. J. Multiph. Flow 22 (1996) 133–155.
- [23] H. Ki, P.S. Mohanty, J. Mazumder, 20th ICALEO 2001, vol. 92 & 93, Congress Proceedings, 2001, pp. 933–942.
- [24] W.D. Bennon, F.P. Incropera, Int. J. Heat Mass Transf. 30 (1987) 2161–2170.
- [25] H. Ki, P.S. Mohanty, J. Mazumder, J. Phys. D Appl. Phys. 34 (2001) 364–372.
- [26] H. Ki, P.S. Mohanty, J. Mazumder, Numer. Heat Transf. Part B 48 (2005) 125–145.
- [27] D. Lee, R. Patwa, H. Herfurth, J. Mazumder, J. Power Sources 210 (2012) 327–338.
- [28] R. Fabbro, K. Chouf, J. Appl. Phys. 87 (2000) 4075–4083.
- [29] S. Asai, I. Muchi, Trans. ISIJ 18 (1978) 90–98.
- [30] H. Ki, Modeling and Measurement of Processes with Liquid–Vapor Interface Created by High Power Density Lasers (2001).
- [31] S. Osher, J.A. Sethian, J. Comput. Phys. 79 (1988) 12–49.
- [32] J.A. Sethian, Level Set Methods and Fast Marching Methods, second ed., Cambridge University Press, Cambridge, 1999.
- [33] S.V. Patankar, Numerical Heat Transfer and Fluid Flow, Hemisphere Pub. Corp., McGraw-Hill, Washington, New York, 1980.
- [34] J.A. Sethian, Level Set Methods and Fast Marching Methods: Evolving Interfaces in Computational Geometry, Fluid Mechanics, Computer Vision, and Materials Science, second ed., Cambridge University Press, Cambridge, U.K., New York, 1999.
- [35] D. Lee, J. Mazumder, in: Proceedings of the ICALEO, Laser Institute of America, Orlando, Florida, 2011.
- [36] M.J. Assael, K. Kakosimos, R.M. Banish, J. Brillo, I. Egry, R. Brooks, P.N. Qusted, K.C. Mills, A. Nagashima, Y. Sato, W.A. Wakeham, J. Phys. Chem. Ref. Data 35 (2006) 285–300.
- [37] B.B. Alchagirov, A.M. Chochaeva, V.B. Bekulov, K.B. Khokonov, High Temp. 41 (2003) 472–476.
- [38] R. Brandt, G. Neuer, Int. J. Thermophys. 28 (2007) 1429–1446.
- [39] E.H. Buyco, F.E. Davis, J. Chem. Eng. Data 15 (1970) 518.
- [40] M. Musella, C. Ronchi, M. Brykin, M. Sheindlin, J. Appl. Phys. 84 (1998) 2530–2537.
- [41] H.R. Leider, O.H. Krikorian, D.A. Young, Carbon 11 (1973) 555–563.
- [42] M. Shusser, J. Appl. Phys. 101 (2007) 033529-1–033536.